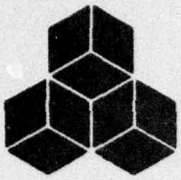

SYSTEMS, SCIENCE AND SOFTWARE

SSS-R-77-3057

THE DEPENDENCE OF BODY WAVE MAGNITUDE ON YIELD FOR UNDERGROUND EXPLOSIONS IN SALT

Topical Report

T. C. Bache
J. T. Cherry
B. F. Mason

Sponsored by

Advanced Research Projects Agency
ARPA Order No. 2551

This research was supported by the Advanced Research Projects Agency of the Department of Defense and was monitored by AFTAC/VSC, Patrick AFB, FL 32925, under Contract No. F08606-76-C-0041.

November 1976

P. O. BOX 1620, LA JOLLA, CALIFORNIA 92038, TELEPHONE (714) 453-0060

AFTAC Project Authorization No. VELA/T/7712/B/ETR

Program Code No. 6H189

Effective Date of Contract: October 1, 1976

Contract Expiration Date: September 30, 1977

Amount of Contract: $374,397

Contract No. F08606-76-C-0041

Principal Investigator and Phone No.
Dr. Thomas C. Bache, (714) 453-0060, Ext. 337

Project Scientist and Phone No.
Dr. Ralph W. Alewine, III, (202) 325-8484

UNCLASSIFIED

SECURITY CLASSIFICATION OF THIS PAGE (When Data Entered)

REPORT DOCUMENTATION PAGE

READ INSTRUCTIONS BEFORE COMPLETING FORM

(14) 1. REPORT NUMBER: SSS-R-77-3057

2. GOVT ACCESSION NO.

(9) 3. RECIPIENT'S CATALOG NUMBER

(6) 4. TITLE (and Subtitle): THE DEPENDENCE OF BODY WAVE MAGNITUDE ON YIELD FOR UNDERGROUND EXPLOSIONS IN SALT

5. TYPE OF REPORT & PERIOD COVERED: Topical Report

6. PERFORMING ORG. REPORT NUMBER: SSS-R-77-3057

(10) 7. AUTHOR(s): T. C. Bache, J. T. Cherry, B. F. Mason

(15) 8. CONTRACT OR GRANT NUMBER(s): F08606-76-C-0041, ARPA Order 2551

9. PERFORMING ORGANIZATION NAME AND ADDRESS: Systems, Science and Software, P. O. Box 1620, La Jolla, California 92038

10. PROGRAM ELEMENT, PROJECT, TASK AREA & WORK UNIT NUMBERS: Program Code No. 6H189, ARPA Order No. 2551

11. CONTROLLING OFFICE NAME AND ADDRESS: VELA Seismological Center, 312 Montgomery Street, Alexandria, Virginia 22314

(11) 12. REPORT DATE: Nov 76

(12) 13. NUMBER OF PAGES: 40 P.

14. MONITORING AGENCY NAME & ADDRESS (if different from Controlling Office)

15. SECURITY CLASS. (of this report): Unclassified

15a. DECLASSIFICATION DOWNGRADING SCHEDULE

16. DISTRIBUTION STATEMENT (of this Report)

Approved for Public Release, Distribution Unlimited.

17. DISTRIBUTION STATEMENT (of the abstract entered in Block 20, if different from Report)

18. SUPPLEMENTARY NOTES

19. KEY WORDS (Continue on reverse side if necessary and identify by block number)

Nuclear Explosion Seismology
Body Wave Magnitude Predictions
Explosion Source Theory

20. ABSTRACT (Continue on reverse side if necessary and identify by block number)

The dependence of body wave magnitude (m_b) on yield for explosions in salt is addressed. The objective is to compare Eurasian explosions in salt to hypothetical explosions in salt at Nevada Test Site (NTS) and to actual NTS explosions in granite. The coupling of the explosion energy into elastic waves is computed with a finite difference program. Four calculations were done in which all material properties were fixed→

DD FORM 1 JAN 73 1473 EDITION OF 1 NOV 65 IS OBSOLETE

388507

UNCLASSIFIED

SECURITY CLASSIFICATION OF THIS PAGE (When Data Entered)

20. ABSTRACT (continued)

except the overburden pressure. While the long period source level is rather insensitive to this parameter, at low confining pressures tension cracks open and the source spectrum becomes strongly peaked near 1 Hz.

Using the computed source functions, theoretical short period seismograms were computed for several paths. An m_b-log yield relationship with slope near unity is found. If the NTS path is characterized by $t^* = 1.06$ and the Eurasian path by $t^* = 0.6$, the m_b - log yield curve for hypothetical NTS salt explosions is 0.5 to 0.6 units below that for otherwise identical Eurasian events. Since our source calculations indicate that granite is a higher coupling medium than salt, a theoretical NTS granite m_b - log yield curve lies midway between the two salt curves.

Theoretical and observed body waves were compared for SALMON. With $t^* = 0.6$ a good fit is obtained for COL, the best of the teleseismic recordings. However, higher t^* values give better agreement with the average m_b based on many observations.

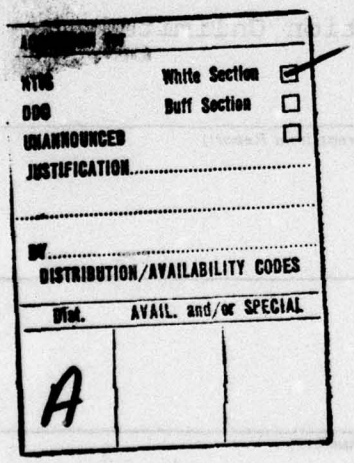

TABLE OF CONTENTS

I. INTRODUCTION

In this report we address the dependence of body wave magnitude (m_b) on yield for explosions in salt. Our objective is to compare salt events in Eurasia to similar, though hypothetical, events at NTS and to granite events at NTS. Our study uses deterministic computational methods and our results are based on time domain measurements from synthetic seismograms. The computational procedure applied is as outlined in previous S^3 reports (e.g., Bache, et al., 1975, 1976; Barker, et al., 1976). The methods have been shown to give theoretical seismograms that agree quite well with observations when the appropriate model parameters are included in the calculations.

The coupling of the explosion-produced shock waves into elastic waves is represented by a reduced displacement potential which provides an equivalent elastic source. A brief description of the constitutive model and material properties for the explosions in salt is given in Section II. Four calculations were carried out in which all material properties were identical except for the overburden pressure which varies proportional to the burial depth. We find that the long period level of the source spectrum is rather insensitive to overburden pressure. However, at the low confining pressures characteristic of shallow burial depths, tension cracks open in the material and the source spectrum is strongly peaked near 1 Hz, the range of interest for body wave magnitude.

In Section III we present our theoretical analysis of the m_b-yield relationships for explosions in salt. We begin by computing theoretical seismograms for a series of explosions varying in yield and burial depth. The source-receiver travel path is meant to be appropriate for explosions in Eurasia. We find an m_b-log yield relationship with slope of about unity, though it can vary from this value depending

on the population being fit. Further, the theoretical m_b values agree rather well with observations.

Our next step was to compute theoretical seismograms for several hypothetical salt events at NTS. For NTS events we have estimates for the source-receiver path characteristics and can accurately predict m_b. The major difference between the NTS and Eurasian path is in the attenuation which is characterized by a parameter called t*. In this case the t* values are 1.06 and 0.6 for the two paths. The m_b-log yield curve for the hypothetical salt events is then 0.5-0.6 m_b units below that for otherwise identical events in Eurasia. We caution that this difference is based on our "first-cut" estimate for the source-receiver path for Eurasian events. But while we are not sure exactly what the m_b difference between identical events at the two sites is, we believe it is substantial.

The next step in our analysis is to compare the m_b-yield data for the salt events to that for events in granite at NTS. We find that the granite m_b-log yield curve lies midway between those for the Eurasian and NTS salt events. This reflects the fact that the granite is a somewhat higher coupling material than the salt.

Finally, we look at the event SALMON, a U.S. explosion in salt. The comparison of theoretical and actual m_b is somewhat ambiguous because of the scatter in the observed values. However, we find that with t* = 0.6 our theoretical seismogram at the best of the teleseismic stations (COL) agrees quite well with the observations. On the other hand, higher t* values give better agreement with the average m_b over the network based on many observations.

II. THE EQUIVALENT ELASTIC SOURCE FOR EXPLOSIONS IN SALT

Coupling of the explosion-produced shock wave was computed with the one-dimensional (spherically symmetric) finite difference code, SKIPPER. Description of the technique and the constitutive models may be found in Cherry, et al. (1975).

The material parameters for the calculation were:

P wave velocity, α = 4.2 km/sec,

S wave velocity, β = 2.41 km/sec,

Density, ρ = 2.15 gm/cm^3,

Porosity, ϕ = 0.0,

Failure envelope parameters:

Y_0 = 0.066 kbar,

Y_m = 0.467 kbar,

$\bar{P}_m$ = 0.42 kbar.

The failure envelope parameters satisfy

$$Y(P) = Y_0 + Y_m \frac{\bar{P}}{\bar{P}_m}\left(2 - \frac{\bar{P}}{\bar{P}_m}\right), \quad \bar{P} < \bar{P}_m ,$$

$$= Y_0 + Y_m, \quad \bar{P} > \bar{P}_m , \tag{2.1}$$

$$\bar{P} = P - \frac{1}{2}\sqrt{\frac{J_3'}{2}} ,$$

where J_3' is the third deviatoric stress invariant and P is the pressure including the overburden. The Y is the maximum stress difference or twice the maximum shear stress. The meaning of these parameters is indicated schematically in Figure 2.1.

These strength parameters give an unconfined compressive strength of 0.411 kb and a maximum allowable stress difference of 0.533 kb.

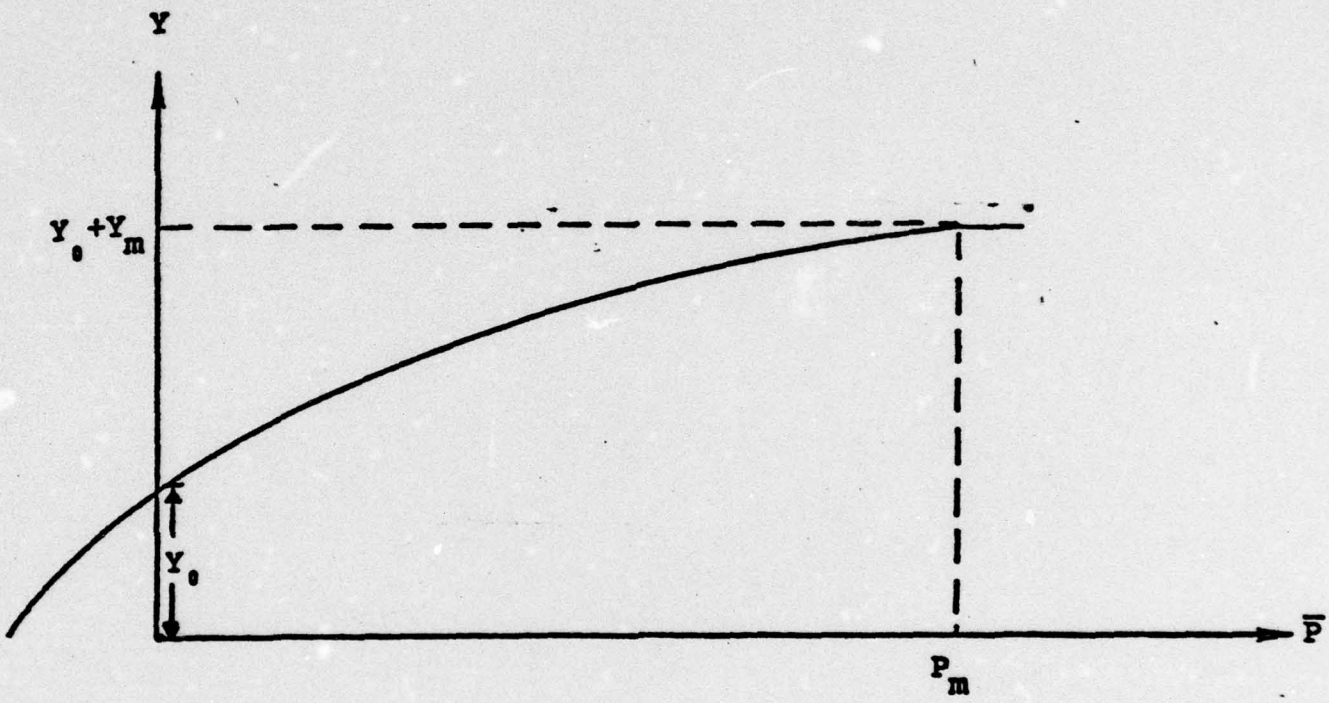

Figure 2.1. Assumed relationship between the material strength (Y) and the hydrodynamic component of stress ($\bar{P}$).

The finite difference calculation of the outgoing shock wave is carried into the elastic regime. From the elastic field an equivalent elastic point source is computed in the form of the reduced displacement potential (Ψ) which is related to the displacement by

$$u(R,t) = \frac{\Psi(\tau)}{R^2} + \frac{\dot{\Psi}(\tau)}{R\alpha} \quad , \tag{2.2}$$

$$\tau = t - R/\alpha \ .$$

A convenient display of the elastic source is given by the amplitude of the Fourier transformed reduced velocity potential, $|\dot{\Psi}(\omega)|$.

Four calculations were carried out with only the overburden pressure varying. Overburden pressure is simply ρgH where H is the explosion burial depth and g is the acceleration of gravity. The source functions for these four calculations are shown in Figure 2.2. Note that the depth varies from quite shallow (0.15 km) to quite deep (2.5 km).

In comparing the source functions in Figure 2.1 there are two frequency ranges of primary interest. The teleseismic surface wave magnitude (M_s) depends on the amplitude of the source function around 0.05 Hz. On the other hand, for m_b the important frequencies are around 1 Hz. The value of the $|\dot{\Psi}(\omega)|$ at these two frequencies is tabulated in Table 2.1.

From the tabulated values we see that the long period level is mildly sensitive to depth, varying by only 20 percent over the entire range. However, the short period level varies by a factor of 2.2 from largest to smallest. This is because of the marked peaking of the source function at shallow depths. This peaking is due to the opening of tensile cracks in the material at low confining pressures.

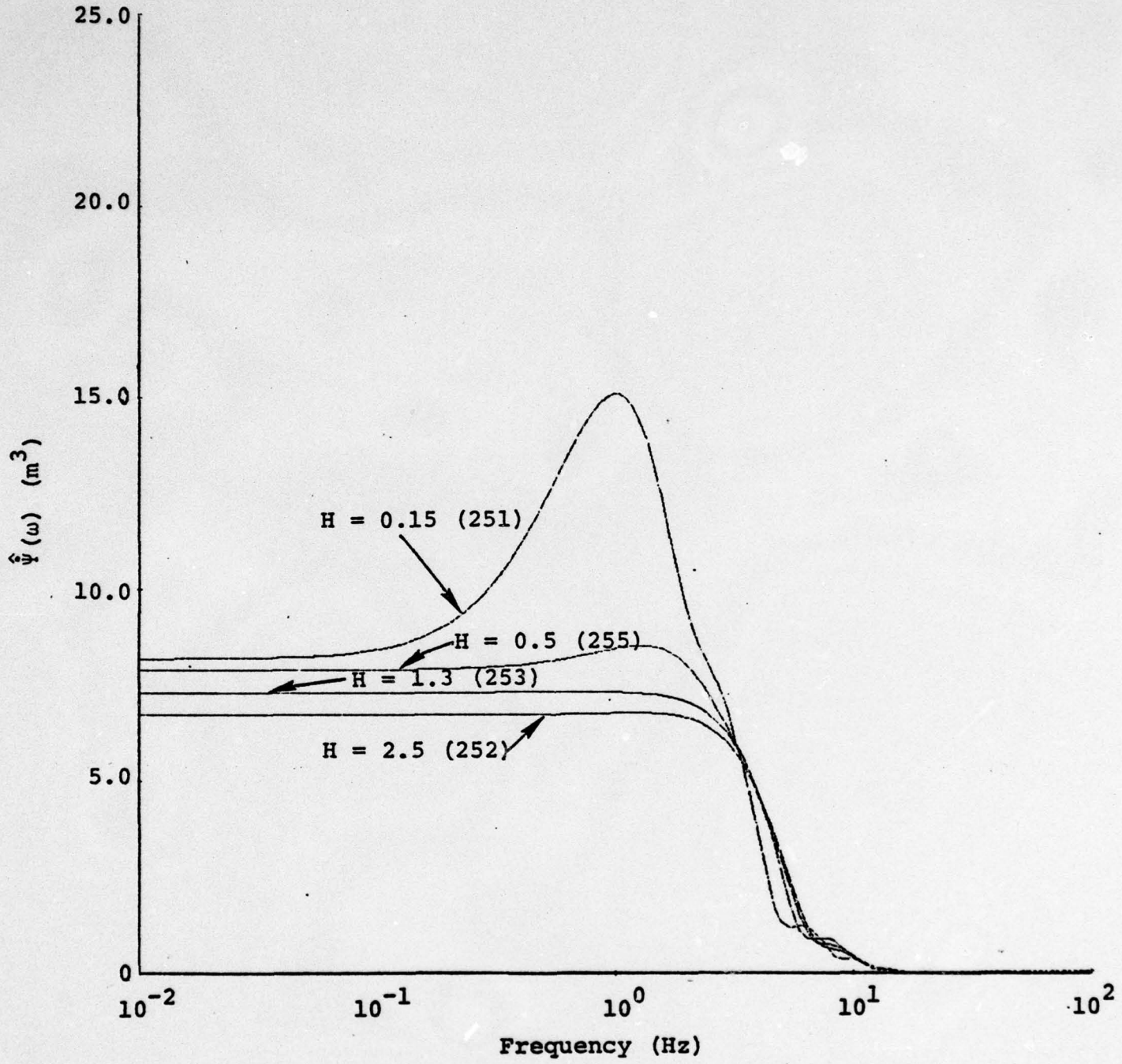

Figure 2.2. Source functions for salt with variable overburden (indicated by the depth H, in km). The frequency axis is scaled to 150 kt, the amplitude axis to 0.02 kt.

In short, the body wave portion of the spectrum is much more sensitive to depth of burial than the long period or surface wave portion.

TABLE 2.1

SOURCE FUNCTION AMPLITUDE AT CHARACTERISTIC BODY AND SURFACE WAVE FREQUENCIES

Source	Depth (km)	$\hat{\dot{\Psi}}$ (.05 Hz, m^3)	$\hat{\dot{\Psi}}$ (1 Hz, m^3)
251	0.15	8.2	15.1
255	0.5	7.9	8.5
253	1.3	7.4	7.4
252	2.5	6.8	6.8

The value of $\Psi(\infty)$ obtained from free field measurements for SALMON (5 kt, 823 m DOB) was approximately 3100 m^3 (Patterson, 1966). This $\Psi(\infty)$ cube root scales to 12.4 m^3 for a yield of 0.02 kt. From Table 2.1 the comparable computed values ($\hat{\dot{\Psi}}$ (0.05 Hz)) is a factor of 1.6 below that for SALMON. This corresponds to a magnitude difference between the SALMON and calculated sources of approximately 0.2 magnitude units.

No material strength data were available for either the GNOME or SALMON salt. The strength parameters used for the source calculations were obtained from Heard, et al. (1975) and Lyuke, et al. (1976). The Lawrence Livermore Laboratory data were obtained from an artificial aggregate of hydrostatically compressed polycrystalline salt with a purity of 99.4 to 99.9 percent. The calculation of the SALMON equivalent source should be performed with strength data appropriate to the SALMON salt.

III. THE DEPENDENCE OF m_b ON YIELD FOR EXPLOSIONS IN SALT

3.1 COMPUTATIONAL METHOD

The computational method for computing body wave seismograms includes the following elements:

1. The reduced displacement potential (RDP) is computed by our one-dimensional finite difference code (SKIPPER). The results were presented in Section II.

2. The RDP is input to a program which computes the detailed crustal reverberations for an equivalent elastic point source at depth in a plane-layered crustal model [Bache and Harkrider, 1976].

3. Crustal reverberations in a plane-layered model of the crust at the receiver are computed using the method of Haskell [1962].

4. The effect of the upper mantle is computed by generalized ray theory as implemented by Helmberger and described in Wiggins and Helmberger [1974].

5. Anelastic attenuation and the attendant dispersion are included via the operator

$$\exp\left[-\pi f\, t^*\left[1 - \frac{2}{\pi}\, i\, \ell n\left(\frac{1000}{f}\right)\right]\right],$$

using the formulation suggested by Strick [1970]. Here f is frequency and the controlling parameter is $t^* = T/Q$, the ratio of travel time to the average path material quality factor.

6. The response of the appropriate instrument is convolved with the ground motion.

3.2 EARTH MODELS

Two models for the source crustal structure were used. These are tabulated in Table 3.1. For the crust in the receiver region a simple model having no important effect on the frequency content of the seismogram was chosen. However, the absolute amplitude is roughly proportional to the inverse of the velocity of the top layer (see Appendix B of Barker, et al. [1976]). This model is tabulated in Table 3.2. The crustal models at the source and receiver accounted for the top 20 km of the earth. We also need a model for the crust and upper mantle below this depth.

The stations of interest for the synthetic seismogram calculations were at great distances from the source (> 45°). At this distance the upper mantle does little more than geometrically spread the single ray that makes up the P wave arrival. The amplitude is controlled by the structure near the turning point which is at great depth (> 1000 km). In selecting an upper mantle model then there are two points to be kept in mind. First, there is little evidence of lateral inhomogeneity in the mantle at these depths. Second, most proposed earth models predict about the same amplitude (geometric spreading) for the distances of interest.

In view of the comments of the previous paragraph, the upper mantle model selected for our calculations was one of the best available average earth models. This model is C2 proposed by Anderson and Hart [1976], which we refer to as C2AH.

The remaining earth model quantity to be selected is t*. For these computations we use t* = 0.6. We believe that t* for Eurasian travel paths is considerably lower than for paths such as NTS-Alaska that we have extensively studied (e.g., Bache, et al., 1977). For the latter paths t* approximately equal to 1.0 is appropriate. The value of 0.6 is an estimate that requires more research for refinement.

TABLE 3.1

SOURCE REGION CRUSTAL MODELS*

Depth (km)	α (km/sec)	β (km/sec)	ρ (gm/cm^3)
Model SS1			
0.1	1.4	0.8	1.6
3.3	4.2	2.4	2.15
5.0	4.6	2.6	2.5
8.0	5.0	2.7	2.7
---	6.0	3.5	2.8
Model SS2			
0.18	1.4	0.8	1.6
0.24	5.0	2.7	2.6
3.3	4.2	2.4	2.15
5.0	4.6	2.6	2.5
8.0	5.0	2.7	2.7
---	6.0	3.5	2.8

*These structures are not meant to represent any particular area but merely to be typical of what is encountered in salt dome regions (e.g., Warren, et al., 1966).

TABLE 3.2

RECEIVER REGION CRUSTAL MODEL

Depth (km)	α (km/sec)	β (km/sec)	ρ (gm/cm^3)
2.58	3.67	2.31	2.40
4.84	5.42	3.27	2.60
11.61	5.80	3.45	2.60
---	6.00	3.50	2.80

3.3 SYNTHETIC SEISMOGRAMS

Synthetic seismograms were computed at two epicentral distances, 56.6° and 66.8°. The parameters for the calculation are summarized in Table 3.3.

Note that the source crustal structure denoted SS2 in Table 3.1 was used for all the synthetic seismograms except the two at the smallest burial depth. For these two the high velocity cap on the salt layer was removed to make up the structure SS1.

We must say a few words about the P-pP lag time in the calculation and its relation to the burial depth. The P and S wave velocities specifying the structures in Tables 3.1 and 3.2 are elastic wave velocities consistent with well log or laboratory measurements. It is well-known that the initial ground motion at ground zero almost always arrives later than would be expected from the sonic velocity logs (the energy travels part of the way as a shock wave with velocity higher than the sound speed). Also, study of the P-pP lag from far-field P wave recordings indicates a greater lag than expected from the elastic analysis (e.g., Springer, 1974). In the elastic analysis the P-pP lag may be computed from

$$\text{P-pP lag} = \sum_{i=1}^{N} \frac{2H_i}{\alpha_i} \cos \theta_i ,$$

$$\theta_i = \sin^{-1} \alpha_i p , \qquad (3.1)$$

where H_i is the thickness of the layer of velocity α_i between the source and the free surface. The ray parameter, p, is determined by the generalized ray theory calculations.

TABLE 3.3

PARAMETERS FOR SYNTHETIC SEISMOGRAM CALCULATIONS

Yield	Depth*	P-pP lag*	Source (Overburden Depth)**	Source Crustal Structure
1	0.165	0.19	251 (0.15)	SS1
8	0.165	0.19	251 (0.5)	SS1
25	0.60	0.50	255 (0.5)	SS2
65	0.60	0.50	255 (0.5)	SS2
15	1.15	0.80	253 (1.3)	SS2
35	1.15	0.80	253 (1.3)	SS2
40	2.4	1.49	252 (2.5)	SS2
65	2.4	1.49	252 (2.5)	SS2
200	1.0	0.72	253 (1.3)	SS2
200	1.5	1.00	253 (1.3)	SS2
200	2.0	1.27	252 (2.5)	SS2
200	2.5	1.55	252 (2.5)	SS2

* The depth used in the calculations was modified to increase the P-pP lag, see the text.

** The source with overburden depth closest to the shot depth was selected since calculations were not done at all source depths.

In this case p = 0.06 sec/km. This corresponds to $\theta = 14.7°$ in the source layer ($\alpha = 4.2$ km/sec).

It is clear from (3.1) that to increase the P-pP lag we must either increase H_i or decrease α_i. The latter change will affect the reflection coefficients as well as the lag. Therefore, we chose to increase the H_i to obtain lags that are somewhat greater than those predicted by the given elastic velocities and depths. For this reason the actual calculations were done with the depth in Table 3.3 multiplied by 1.2.

The computed synthetic seismograms are shown in Figures 3.1 and 3.2. The source function, yield and depth for each calculation is printed on the records. Also appearing on the records are the m_b values from measurements of the b and A phases. The b phase is the first cycle on the record. The A phase is the maximum phase in the first few cycles and is indicated with a bar. The m_b is computed from

$$m_b = \log \frac{A}{T} + B, \tag{3.2}$$

where B is taken to be 3.5 for the station at 56.6° and 3.7 for the station at 66.8°. The amplitude in (3.2) is measured peak-to-peak. Given in parentheses with each m_b is the period of the cycle measured. The period is seen to be dependent on the explosion depth and yield. The raw data for the seismograms of Figures 3.1 and 3.2 is summarized in Table 3.4.

3.4 THE DEPENDENCE OF m_b ON YIELD

The next step is to examine the dependence of m_b on yield. For this purpose we plot m_b versus log W for m_b^A

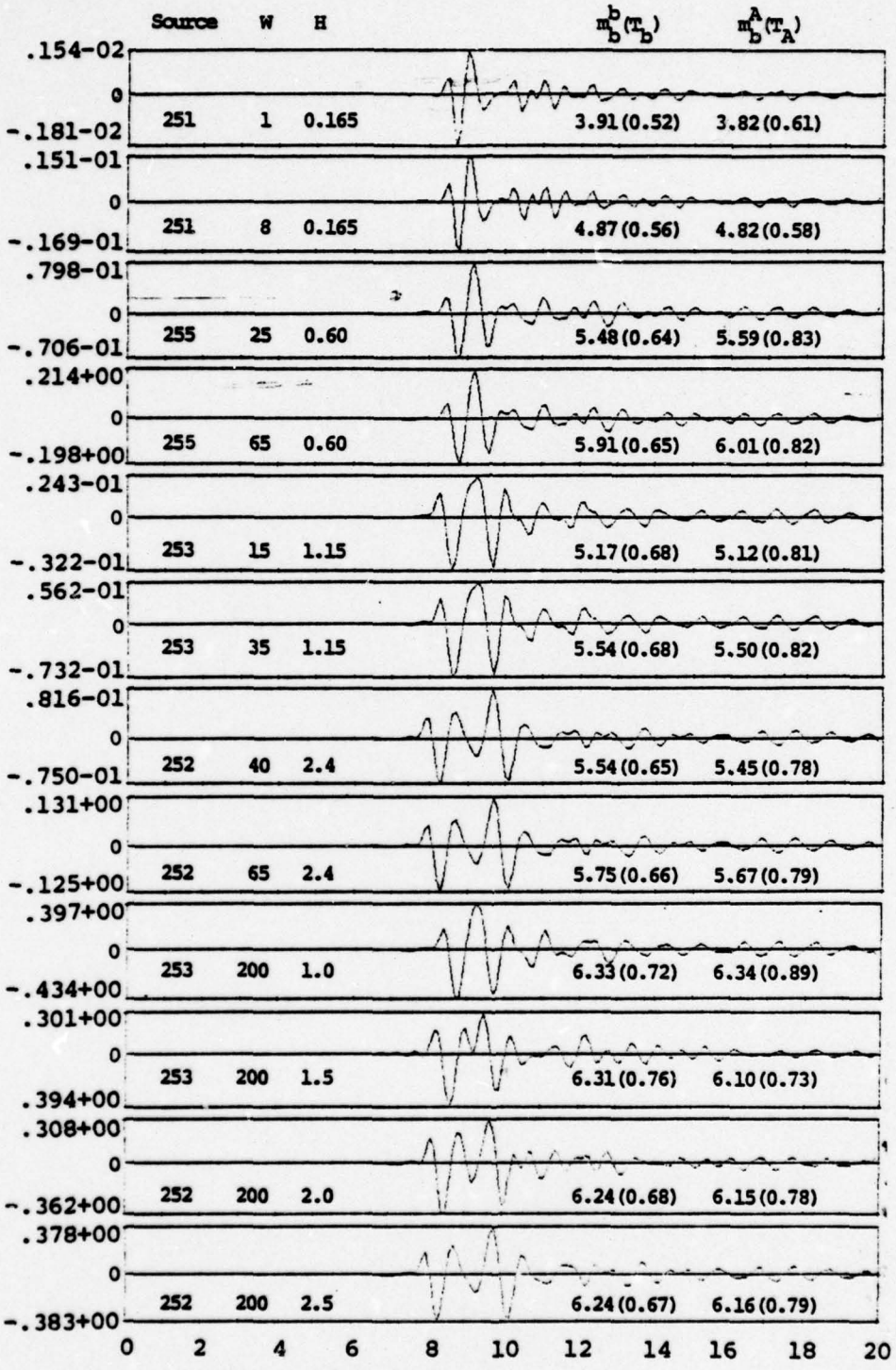

Figure 3.1. Synthetic seismograms at 56.6°. The numbers at the left are ground motion in microns at 1 Hz.

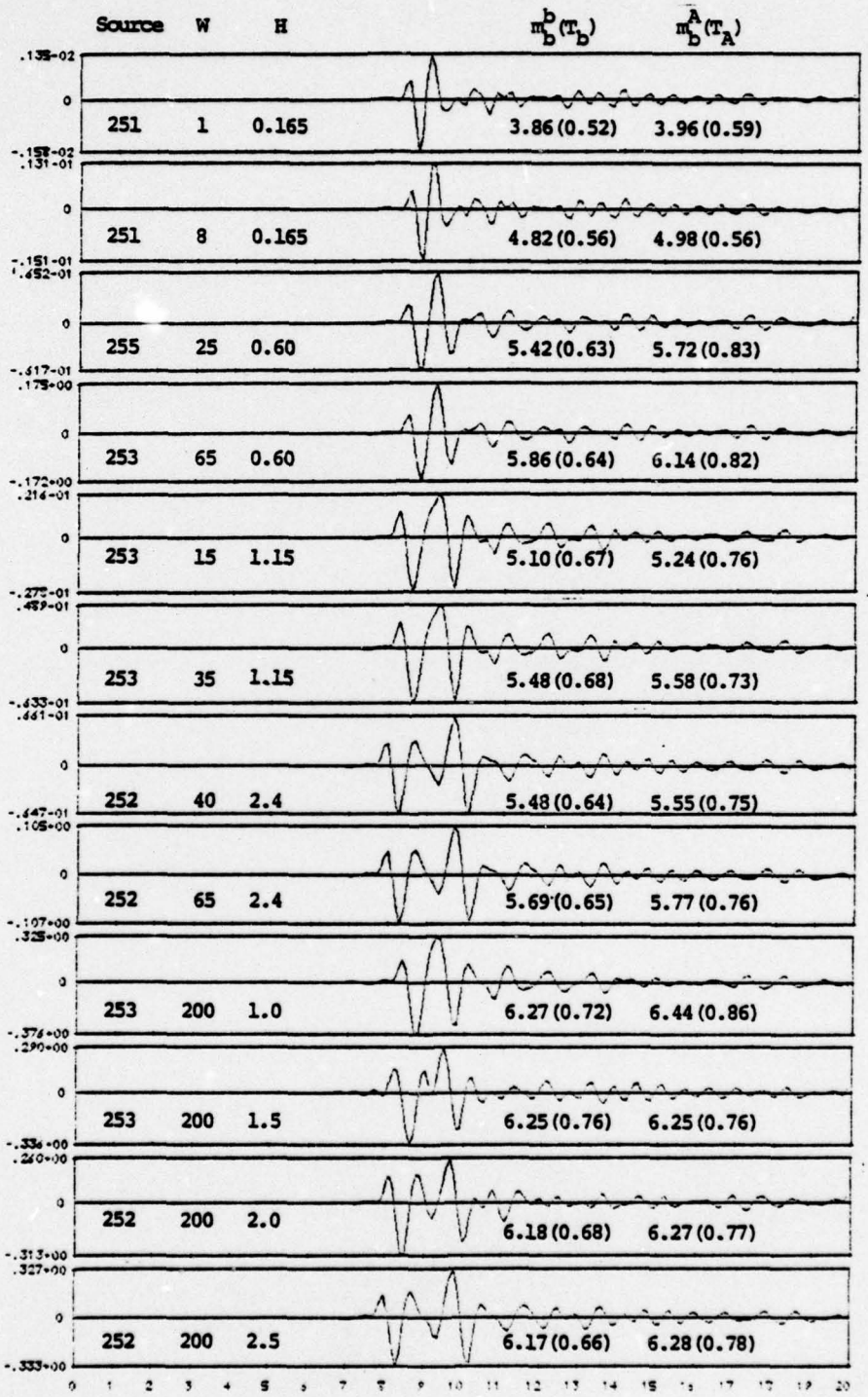

Figure 3.2. Synthetic seismograms at 66.8°.

TABLE 3.4

AMPLITUDE/PERIOD DATA FOR THE SYNTHETIC SEISMOGRAMS OF FIGURES 3.1 AND 3.2

Yield	P-pP Lag	b	T_b	A	T_A
Range = 56.6° (B = 3.5)					
1	0.19	0.85	0.52	1.27	0.61
8	0.19	8.32	0.56	12.0	0.58
25	0.50	38.7	0.64	103.0	0.83
65	0.50	107.0	0.65	266.0	0.82
15	0.80	20.1	0.68	34.1	0.81
35	0.80	46.6	0.68	81.5	0.82
40	1.49	44.7	0.65	69.4	0.78
65	1.49	74.1	0.66	117.0	0.79
200	0.72	308.0	0.72	632.0	0.89
200	1.00	311.0	0.76	293.0	0.73
200	1.27	237.0	0.68	351.0	0.78
200	1.55	230.0	0.67	362.0	0.79
Range = 66.8° (B = 3.7)					
1	0.19	0.75	0.52	1.07	0.59
8	0.19	7.36	0.56	10.6	0.56
25	0.50	33.3	0.63	86.8	0.83
65	0.50	91.9	0.64	224.0	0.82
15	0.80	16.9	0.67	26.1	0.76
35	0.80	40.6	0.68	55.7	0.73
40	1.49	38.4	0.64	52.6	0.75
65	1.49	63.7	0.65	88.7	0.76
200	0.72	267.0	0.72	474.0	0.86
200	1.00	269.0	0.76	269.0	0.76
200	1.27	206.0	0.68	284.0	0.77
200	1.55	196.0	0.66	295.0	0.78

and m_b^b at the two ranges. The best least squares linear fit to the data was computed giving relations of the form

$$m_b = a_1 \log W + a_2. \tag{3.3}$$

The regression was done assuming no error in the yield values. The results are summarized in Table 3.5. In Figures 3.3-3.4 the m_b^A is plotted for the two stations.

The m_b-log yield values are separated into two groups according to their scaled depth of burial. The shallow events have scaled depths $D \in [82.5, 205]$, where the actual depth $H = DW^{1/3}$. The deeply buried events have D varying between 351 and 701 meters.

From the graphs and Table 3.5, we see that there is almost no difference between the seismograms at the two ranges. At these ranges the upper mantle spreading is nearly independent of frequency and proportional to Δ^{-1}. This spreading gives log A/T values at the farther station that are about 0.07 smaller than those at the nearer station. However, the distance correction (B) differs by 0.2 magnitude units. That is, the amplitude decay predicted by the upper mantle model is not consistent with the variation of B in this distance range. Thus, the magnitude at the farther station should be about 0.13 magnitude units larger than that at the nearer and this is consistent with the values we get.

3.5 COMPARISON TO OBSERVATIONS

Several of the theoretical events are similar in depth and yield to actual events. The m_b for these events can be compared to the theoretical values plotted in Figures 3.3 and 3.4. The agreement between the theoretical and actual m_b is generally quite good.

3.6 COMPARISON TO HYPOTHETICAL SALT EVENTS AT NTS

We have a well-developed capability to compute theoretical seismograms for NTS events that have m_b quite close

TABLE 3.5

BEST LINEAR RELATIONS FOR THE DATA OF FIGURES 3.1 AND 3.2

Data Set		
$\Delta = 56.6°$		
Entire set	$m_b^b = 1.02 \log W + 3.95$	$m_b^A = 1.01 \log W + 3.93$
$D \in [82.5, 205]$	$m_b^b = 1.07 \log W + 3.93$	$m_b^A = 1.14 \log W + 3.86$
$D \in [351, 701]$	$m_b^b = 0.95 \log W + 4.05$	$m_b^A = 0.92 \log W + 4.03$
$\Delta = 66.8°$		
Entire set	$m_b^b = 1.02 \log W + 3.90$	$m_b^A = 1.00 \log W + 4.06$
$D \in [82.5, 205]$	$m_b^b = 1.07 \log W + 3.88$	$m_b^A = 1.12 \log W + 4.01$
$D \in [351, 701]$	$m_b^b = 0.95 \log W + 3.99$	$m_b^A = 0.92 \log W + 4.12$

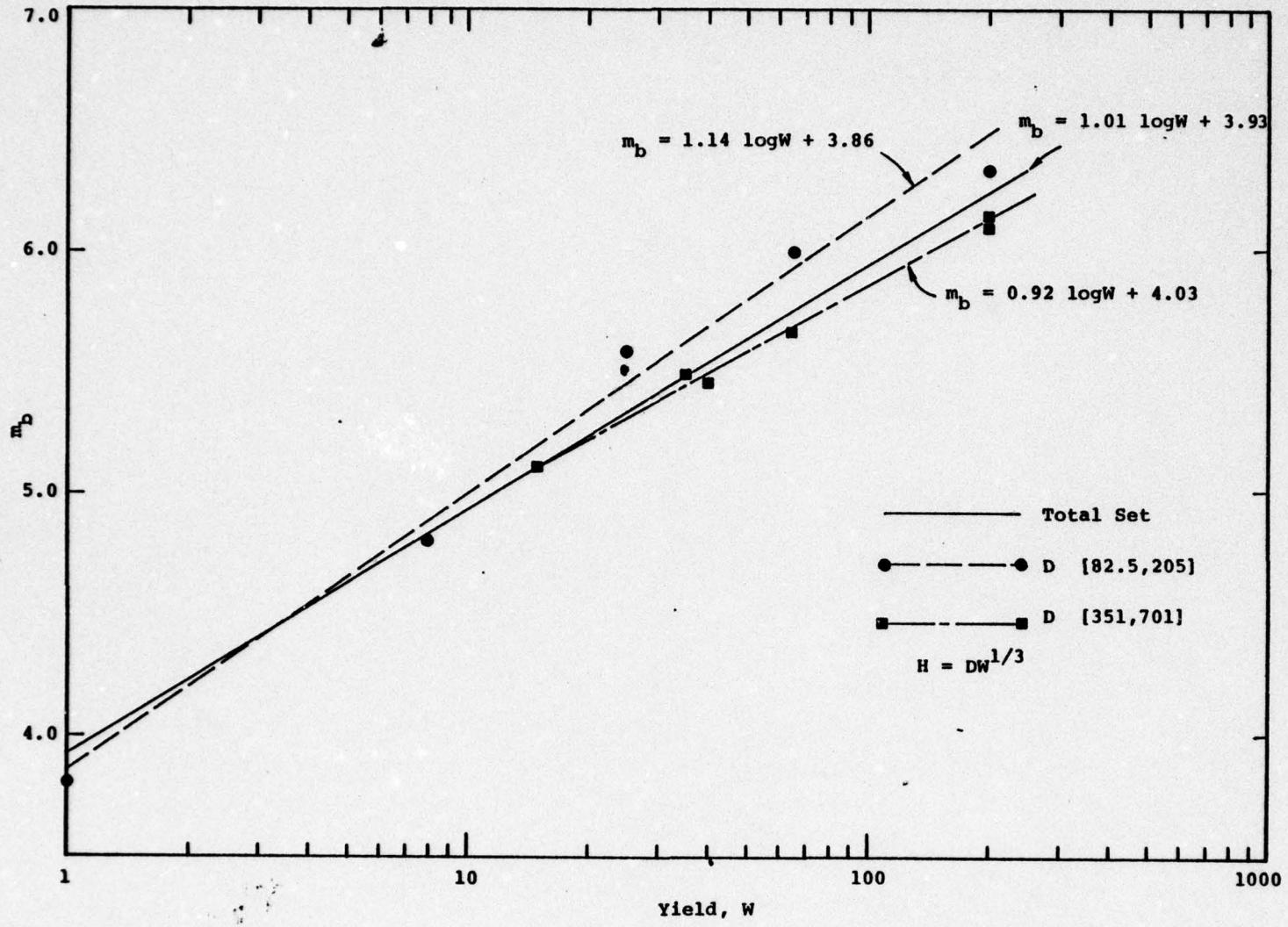

Figure 3.3. m_b^A versus yield at 56.6°. Least square lines are fit to the total data set and to two subgroups divided by scaled depth of burial.

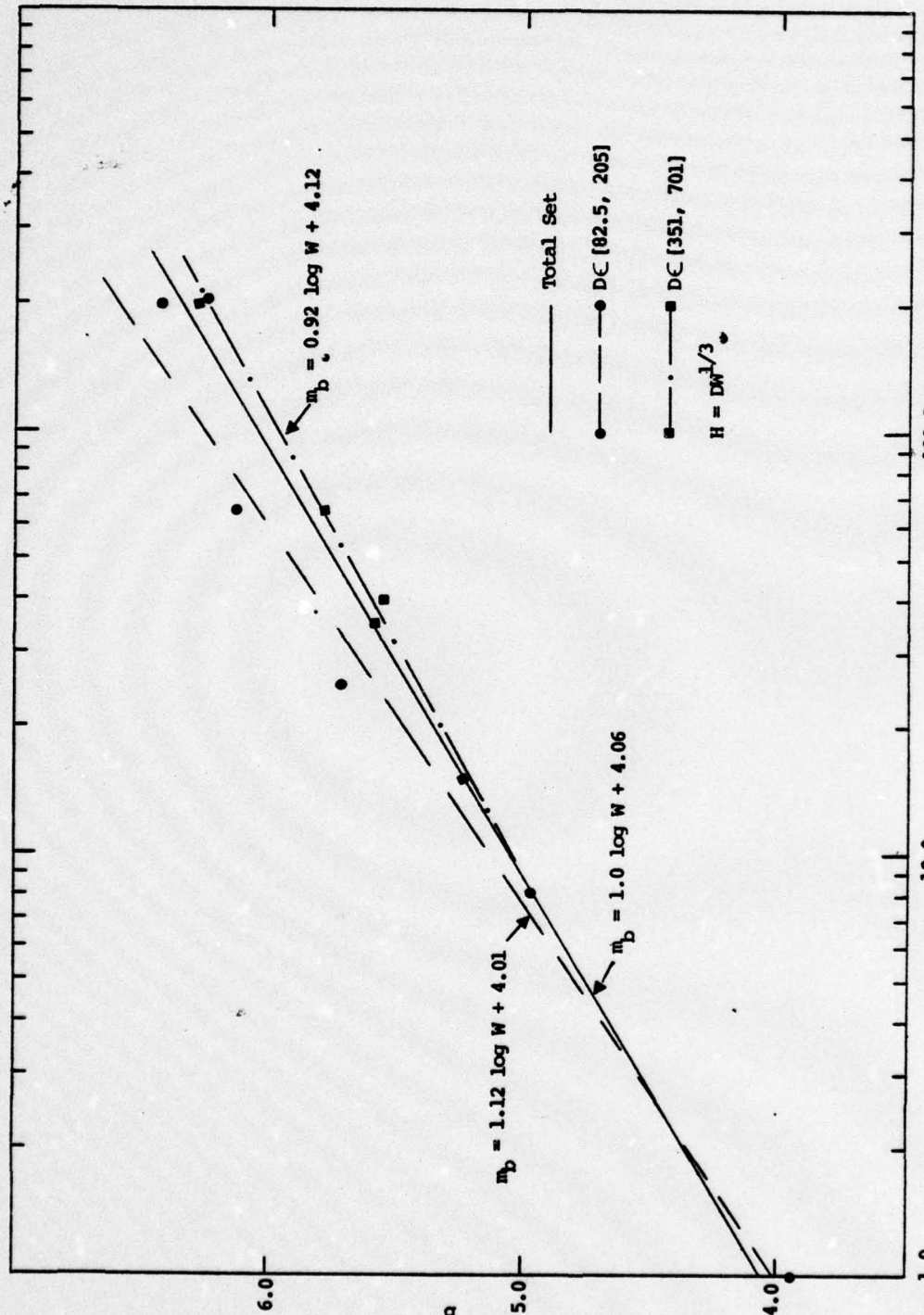

Figure 3.4. m_b^A versus yield at 66.8°. Least square lines are fit to the total data set and to two subgroupings divided by scaled depth of burial.

to that observed. Therefore, let us construct theoretical seismograms for events just like those discussed in the previous section, changing the path parameters to be appropriate for NTS events. Once again the upper mantle model C2AH is used, but the range is 33.4°. The t* = 1.06. With these path parameters a B value of 3.32 gives theoretical m_b that closely agree with network averages for NTS events.

Theoretical seismograms for hypothetical NTS salt events were computed for five of the twelve events described in Table 3.3. The seismograms are shown in Figure 3.5. The data is summarized in Table 3.6. These data should be compared to the corresponding data in Table 3.4.

The m_b for the NTS travel path events are compared to those for the Eurasian travel path events in Table 3.7. The comparison is given for both the m_b^b and m_b^A values. The difference is computed using the average for the two Eurasian travel paths. Except for the shallow low yield event, the m_b^b difference is fairly constant, varying by less than 0.1. For m_b^A the 15 kt event is also anomalous because the apparent period of the A phase is quite large due to the smooth interference between P and pP at the low t*. The instrument response correction is based on this large apparent period and causes the m_b^A for the NTS path to be artifically large.

3.7 COMPARISON TO EVENTS IN GRANITE

It is interesting to compare m_b-yield for the salt events to that for explosions in granite. The representative event in granite is PILEDRIVER. We have computed synthetic seismograms for PILEDRIVER in the past (e.g., Bache, et al. [1975]) and obtain a theoretical m_b^A of 5.55. The calculation used t* = 1.06 and the same NTS - 33.4° path as the seismograms in the previous section.

Let us first point out the major factors influencing the theoretical m_b for PILEDRIVER. Our one-dimensional

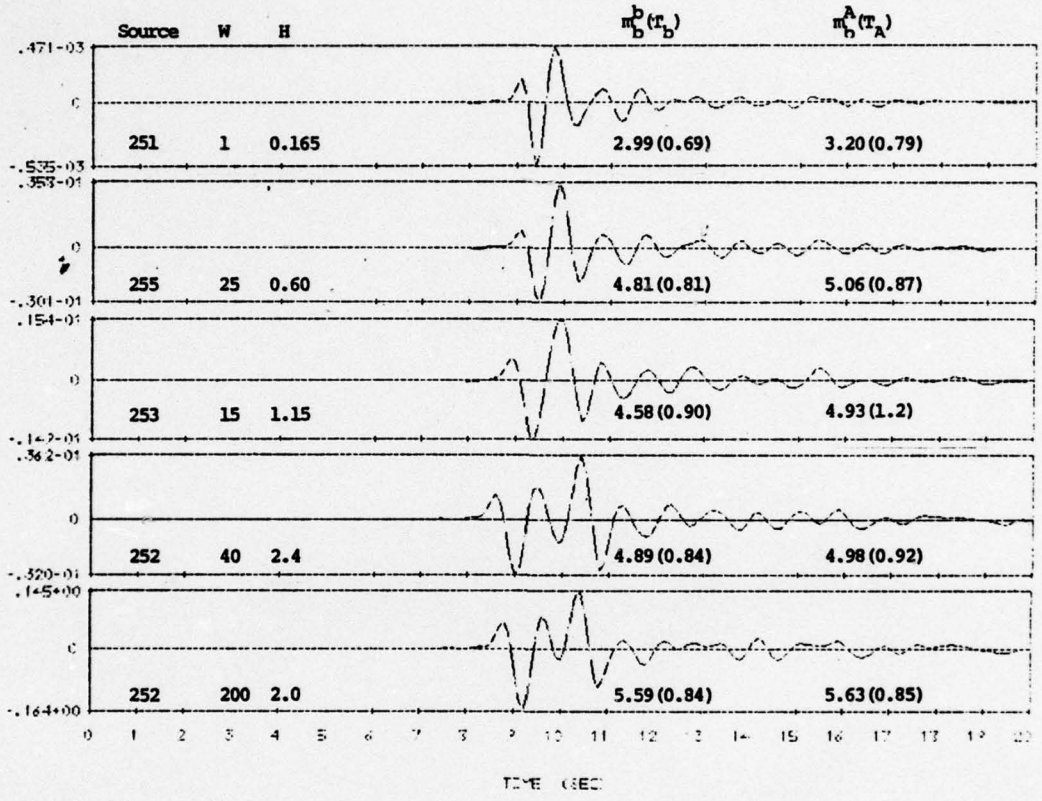

Figure 3.5. Theoretical seismograms for hypothetical events in salt at NTS. The source parameters are the same as for the corresponding Eurasian salt events studied in previous sections. The path parameters are appropriate for an NTS-Alaska path.

TABLE 3.6

AMPLITUDE/PERIOD DATA FOR THE SYNTHETIC SEISMOGRAMS OF FIGURE 3.5

Yield	P-pP Lag	b	T_b	A	T_A
Range = 33.4° (B = 3.32)					
1	0.19	0.32	0.69	0.59	0.79
25	0.50	24.6	0.81	48.1	0.87
15	0.80	16.2	0.89	47.8	1.17
40	1.49	30.8	0.84	42.2	0.92
200	1.27	157.0	0.84	173.0	0.85

TABLE 3.7

COMPARISON OF m_b FOR NTS AND EURASIAN TRAVEL PATHS

Yield	Eurasian Paths Δ=56.6°	Eurasian Paths Δ=66.8°	NTS Path Δ=33.4°	Difference
m_b^A				
1	3.82	3.96	3.20	0.69
25	5.59	5.72	5.06	0.59
15	5.12	5.24	4.98	0.20
40	5.45	5.55	4.98	0.52
200	6.15	6.27	5.63	0.58
m_b^b				
1	3.91	3.86	2.99	0.90
25	5.48	5.42	4.81	0.64
15	5.17	5.10	4.58	0.56
40	5.54	5.48	4.89	0.62
200	6.24	6.18	5.59	0.62

source calculation for PILEDRIVER gives a source function that is larger than that for salt. This is illustrated in Figure 3.6 where the largest (251) and smallest (252) of the salt source functions are compared to that for PILEDRIVER granite. All other things being equal, we expect the amplitude of the telsesismic body waves to scale with $\alpha_s \hat{\Psi}^e$ where α_s is the source region P wave velocity and $\hat{\Psi}^e$ is the amplitude of the source spectrum at the appropriate frequency, about 1 Hz. For salt, α_s = 4.2 km/sec and for granite α_s = 5.3 km/sec. From this first-order scaling we would expect the granite body wave amplitude to be a factor of 2-3 higher than that for otherwise identical events in salt.

The pronounced peak in the PILEDRIVER source function is clearly responsible for much of the coupling difference between the PILEDRIVER granite and the salt. This peaking is caused by several peculiarities of the PILEDRIVER granite -- particularly the presence of water and pre-existing cracks in the granite (see Bache, et al., 1975). These conditions need not apply at other granite sites or at greater depths at the same site.

A second factor strongly controls the PILEDRIVER m_b. This event is characterized by an exceptionally small lag between P and pP. This causes destructive interference and a smaller m_b than expected from source coupling alone.

In order to construct an m_b-yield curve for granite similar to those shown for salt, we need several more granite source functions that take account of the depth effects on source coupling. While these calcualtions are in progress, we can anticipate pretty closely what the results will be. As we increase the depth, the source function would get smaller because of the increasing overburden pressure. We also might reasonably reduce the amount of precracking in the material. In any case, the major effect would be on

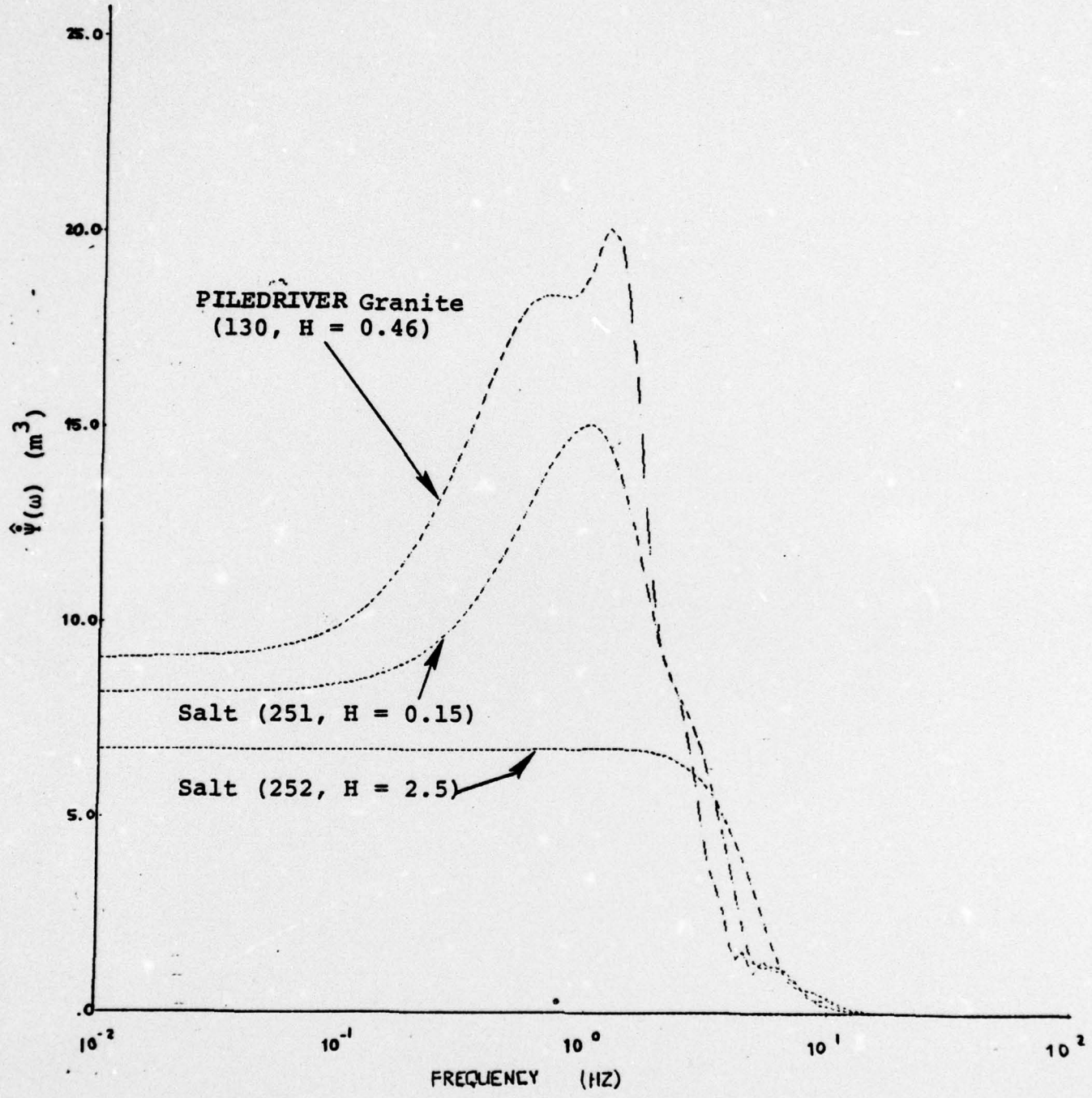

Figure 3.6. The PILEDRIVER source function compared to the largest and smallest of the salt source functions from Figure 2.2. The frequency axis is scaled to 150 kt, the amplitude axis to 0.02 kt.

the 1 Hz portion of the spectrum which would be substantially reduced with increasing depth as was the case for salt (Figure 2.1). At the same time the amount of destructive interference between P and pP becomes less with depth. The result should be an m_b log W curve that has slope of nearly unity.

The m_b-yield values for salt-Eurasian travel path, salt-NTS travel path and PILEDRIVER granite-NTS travel path are compared in Figure 3.7. Three lines of unit slope are shown through the data. The upper most line is the least squares fit to the twelve salt-Eurasian path events plotted in Figures 3.3 and 3.4. The m_b values are the average values from the two stations. The lowest line is 0.55 magnitude units below the salt-Eurasian path line. This is representative of the difference between the salt-Eurasian path and salt-NTS path m_b values compared in Table 3.7.

The unit slope line through the PILEDRIVER theoretical m_b falls almost equidistent between the lines for the two populations of salt events. That is to say, events like PILEDRIVER are expected to give m_b values that are, on the average, 0.1-0.3 magnitude units above those for similar NTS events in salt. On the other hand, the PILEDRIVER-like events give m_b values that are about 0.1-0.3 units lower than Eurasian salt events.

3.8 SALMON

There has been one U.S. explosion in salt that was fairly well recorded teleseismically. This is the ≈ 5 kt explosion SALMON in Mississippi. While discussing salt explosions we should compare our theoretical seismograms to those for SALMON.

Synthetic seismograms were computed for SALMON at $\Delta = 48.8°$. The source region crustal structure is tabulated in Table 3.8. The receiver region structure is the same as

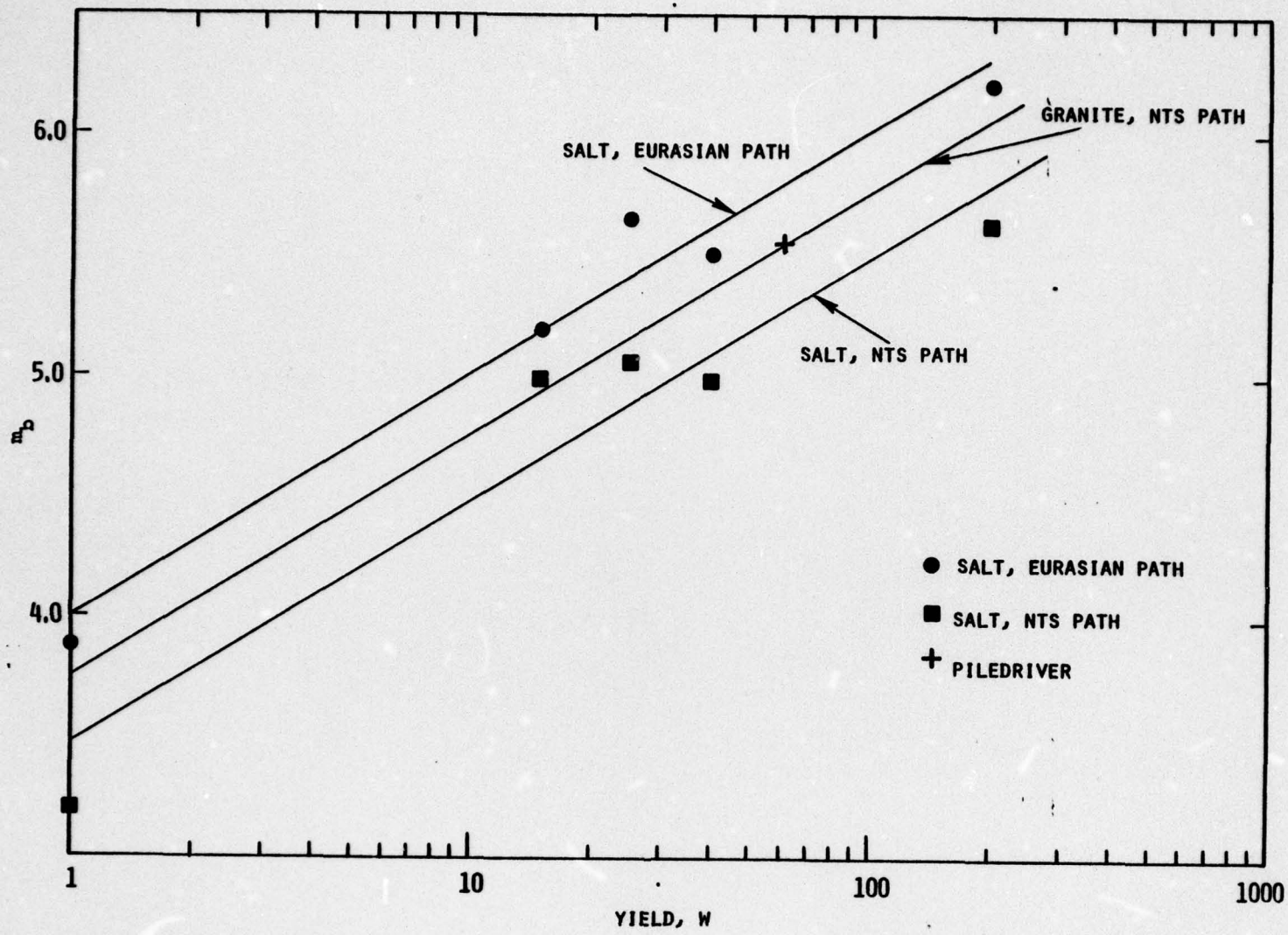

Figure 3.7. Comparison of m_b-yield for salt events in Eurasia and at NTS to granite explosions at NTS.

TABLE 3.8

SOURCE REGION CRUSTAL STRUCTURE FOR SALMON*

Depth (km)	α (km/sec)	β (km/sec)	ρ (gm/cm^3)
0.12	2.1	0.75	1.7
0.37	3.3	1.64	1.8
0.62	4.8	2.7	2.54
2.62	4.2	2.4	2.15
4.0	4.6	2.6	2.5
8.0	5.0	2.7	2.7
---	6.0	3.5	2.8

*Compiled from data given by Rogers [1966] and Warren, et al., [1966].

that used in all calculations in this report, that specified in Table 3.2.

The actual depth of SALMON was 0.83 km. This depth is midway between those for the salt source functions 253 and 255. We chose to compute seismograms using 255, the larger of the two. For the actual seismogram calculations we again increased the depth, this time by 28 percent to 1.06 km. The result is a P-pP delay of 0.56 sec. This is nearly the same as the delay time of 0.58 seconds estimated by Springer [1974] from the arrival time at ground zero.

The earth model for the upper mantle path was again C2AH, this time with $\Delta = 48.8°$ (P = 0.072 sec/km), the range from SALMON to the WWSSN station at College, Alaska (COL). As was the case with the Eurasian paths, it is difficult to confidently select t* for this unfamiliar travel path. We suspect that the appropriate value is smaller than for NTS events. Seismograms were computed for several values of t*. The standard WWSSN seismograph response was convolved with the ground motion.

The theoretical seismograms for SALMON are shown in Figure 3.8. The data from the seismograms is summarized in Table 3.9. For the m_b calculations B = 3.5.

How do the theoretical seismograms compare with observations? The teleseismic observations of SALMON are summarized by Jordan, et al. [1966]. The magnitude values given by these authors are shown plotted versus distance in Figure 3.9. Restricting attention to those values beyond 16°, the average magnitude is found to be $m_b = 4.35$. However, most of the teleseismic magnitudes ($\Delta = 30°$) fall above this average value.

Jordan, et al. show seismograms for a number of teleseismic stations. The best recording is that at COL, the

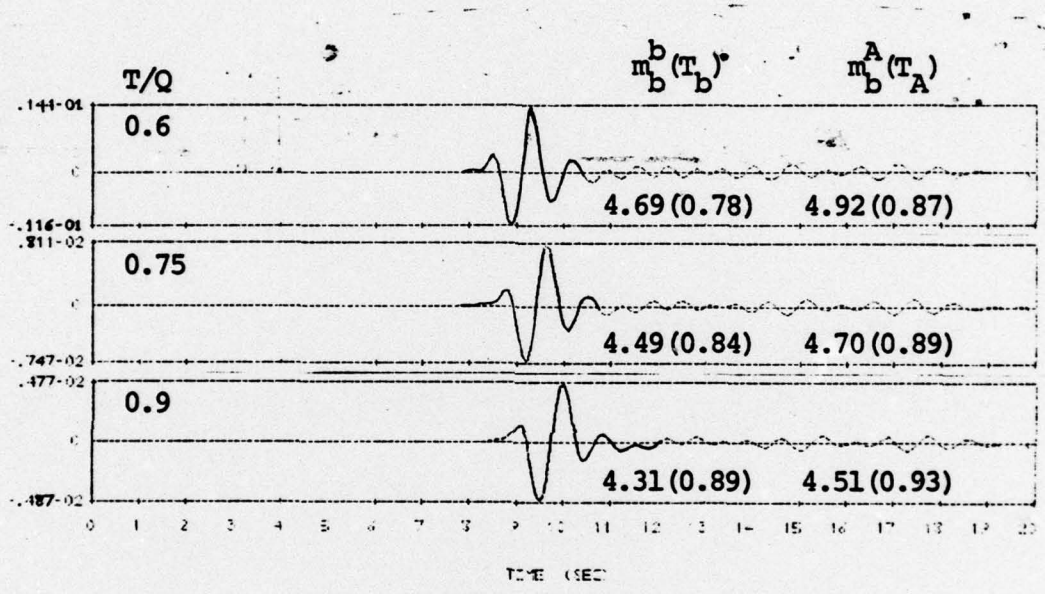

Figure 3.8. Synthetic seismograms for SALMON at Δ = 48.8°.

TABLE 3.9

AMPLITUDE/PERIOD DATA FOR THE SALMON SYNTHETIC SEISMOGRAMS

T/Q	b	T_b	m_b^b	A	T_A	m_b^A
0.6	10.5	0.78	4.63	20.1	0.87	4.86
0.75	7.2	0.84	4.43	12.4	0.89	4.64
0.9	5.0	0.89	4.25	8.3	0.93	4.45

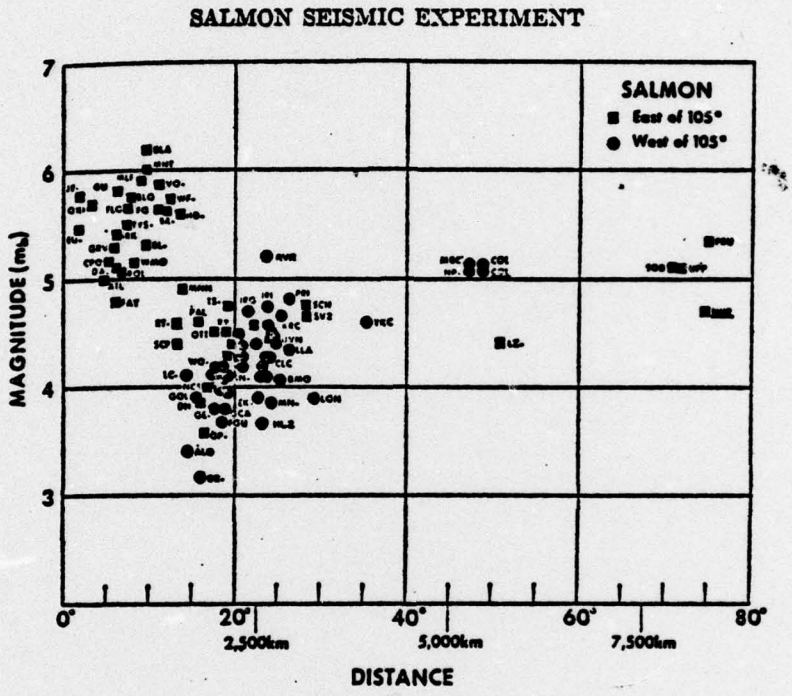

Figure 3.9. Magnitude determinations for the SALMON event (from Jordan, et al. [1966]).

station for which our synthetics were computed. At this station A = 20.5, T_A = 0.8 and m_b^A = 4.97.* Comparing to the data of Table 3.9, we see that the theoretical seismogram with T/Q = 0.6 is in excellent agreement with the observation. On the other hand, higher values of t* give better agreement with the average m_b for the event.

*Jordan, et al. use B = 3.7 at this distance, a value not in agreement with the LRSM shot report tables.

REFERENCES

Anderson, D. L. and R. S. Hart [1976], "An Earth Model Based on Free Oscillations and Body Waves," JGR, 81, pp. 1461-1475.

Bache, T. C., T. G. Barker, N. Rimer and J. M. Savino [1976], "Comparison of Theoretical and Observed Body and Surface Waves from KASSERI, an Explosion at NTS," Systems, Science and Software Topical Report, AFTAC/VSC, SSS-R-76-2937, May.

Bache, T. C. and D. G. Harkrider [1976], "The Body Waves Due to a General Seismic Source in a Layered Earth Model: 1. Formulation of the Theory," BSSA (in press).

Bache, T. C., J. T. Cherry, N. Rimer, J. M. Savino, T. R. Blake, T. G. Barker and D. G. Lambert [1975], "An Exploration of the Relative Amplitudes Generated by Explosions in Different Test Areas at NTS," Systems, Science and Software Final Report (Draft), SSS-R-76-2746, October.

Bache, T. C., J. M. Savino, M. Baker and P. L. Coleman [1977], "Seismic Studies for Improved Yield Determination; Section 3.2: Body Wave Attenuation Properties for Selected Travel Paths," Systems, Science and Software Quarterly Report submitted to AFTAC/VSC, SSS-R-77-3108, January.

Barker, T. G., T. C. Bache, N. Rimer, J. T. Cherry and J. M. Savino [1976], "Prediction and Matching of Teleseismic Ground Motion (Body and Surface Waves) from the NTS MAST Explosion," Systems, Science and Software Technical Report, SSS-R-76-2727.

Cherry, J. T., N. Rimer and W. O. Wray [1975], "Seismic Coupling from a Nuclear Explosion: The Dependence of the Reduced Displacement Potential on the Non-linear Behavior of the Near Source Rock Environment," Systems, Science and Software Topical Report, SSS-R-76-2742, September.

Haskell, N. A. [1962], "Crustal Reflection of Plane P and SV Waves," JGR, 72, pp. 2583-2587.

Heard, H. C., A. E. Abey, B. P. Bonner and A. Duba [1975), "Behavior of Polycrystalline NaCl to 3.2 GPa," Lawrence Livermore Laboratory Report UCRL-51743, January.

REFERENCES (continued)

Jordan, J. N., W. V. Mickey, Wayne Heterbran and D. M. Clark [1966], "Travel Times and Amplitudes from the SALMON Explosion," JGR, 71, pp. 3469-3482.

Lyuke, E. I., S. K. Daragen, V. E. Peregontseva [1976], "Forecasting the Seismic Wave Spectra of Powerful Underground Detonations From the Spectra of Small Preliminary Detonations," Izv. Earth Physics, 2, pp. 39-49.

Patterson, D. W. [1966], "Nuclear Decoupling, Full and Partial," JGR, 71, pp. 3427-3436

Roger, L. A. [1966], "Free-Field Motion Near a Nuclear Explosion in Salt: Project SALMON," JGR, 71, pp. 3415-3426.

Springer, D. L. [1974], "Secondary Sources of Seismic Waves from Underground Nuclear Explosions," BSSA, 64, pp. 581-594.

Strick, E. [1970], "A Predicted Pedestal Effect for Pulse Propagation in Constant-Q Solids," Geophysics, 35, pp. 387-403.

Warren, D. H., J. H. Healy and W. H. Jackson [1966], "Crustal Seismic Measurements in Southern Mississippi," JGR, 71, pp. 3437-3458.

Wiggins, R. A. and D. V. Helmberger [1974], "Synthetic Seismogram Computation by Expansion in Generalized Rays," Geophys. J. R. Astr. Soc., 37, pp. 73-90.